ORNL/SPR-2024/3325
Rev. 1

Characterization of Large Batch 14YWT Heat (NFA-2) for JOYO Irradiations

Nuclear Technology Research and Development

Prepared for US Department of Energy
Nuclear Technology R&D Advanced Fuels Campaign

Caleb Massey and David Hoelzer

Oak Ridge National Laboratory

March 29, 2024

M3FT-24OR020302032

ACKNOWLEDGMENTS

This research was sponsored by the Advanced Fuels Campaign Program of the US Department of Energy (DOE) Office of Nuclear Energy. The report was authored by UT-Battelle LLC under Contract No. DE-AC05-00OR22725 with DOE. The authors would like to acknowledge Cody Taylor for his diligent work in collecting high-temperature mechanical testing data, as well as Jim Horenburg for his mettalography support.

SUMMARY

The development and deployment of advanced cladding materials in advanced reactors requires the collection of relevant performance data for each cladding concept. Novel cladding concepts typically undergo significant innovation and iteration over the course of their development, and intention should be given to providing a snapshot of present performance. Thus, a modern heat of the nanostructured ferritic alloy (NFA) 14YWT is produced using state-of-the-art procedures for impurity minimization combined with thermomechanical processing methods designed to optimize fracture toughness, tensile strength, and ductility. This new heat of 14YWT, NFA-2, will provide the Advanced Fuels Campaign with adequate material for upcoming irradiation and mechanical testing campaigns. This report outlines procurement of new gas atomized 14YWT powder, production of four new bars of 14YWT, and subsequent mechanical and microstructural property characterization.

CONTENTS

FIGURES

TABLES

ACRONYMS

AFC	Advanced Fuels Campaign
BF	bright field
DOE	US Department of Energy
EBSD	electronic backscatter diffraction
EFTEM	energy-filtered TEM
FFT	fast Fourier transform
FWHM	full-width half-maximum
GND	geometrically necessary dislocation
ICP-MS	inductively coupled plasma mass spectrometry
ICP-OES	inductively coupled plasma optical emission spectroscopy
IGF	inert gas fusion
IPF	inverse pole figure
JOYO	Japanese experimental fast reactor
NC	nanocluster
NFA	nanostructured ferritic alloy
ODS	oxide dispersion strengthened
ORNL	Oak Ridge National Laboratory
ROI	region of interest
TEM	transmission electron microscopy

1. Introduction

Oxide dispersion strengthened (ODS) iron-based alloys are widely considered the gold standard advanced cladding concept to be deployed as fast-reactor cladding and are also used for other core materials because of their beneficial high-temperature mechanical properties and irradiation resistance. Specifically, because of their particularly fine precipitate and grain structure, one specific class of ODS alloys, designated as *nanostructured ferritic alloys* (NFAs), have been under development for the past two decades. To achieve high-temperature strength, NFAs contain a high concentration of titanium-, yttrium-, and oxygen-enriched nanoclusters (NCs), ultra-fine grains [1] and creep properties. They also possess high sink strength for trapping irradiation-induced point defects to minimize hardening [2] and swelling. The leading NFA candidate, 14YWT, was first developed in 2001 through funding for nuclear energy projects and laboratory directed research; subsequently, 14YWT quickly grew in popularity as irradiation studies confirmed the alloy's thermal stability and also illustrated its remarkable resistance to irradiation-induced cavity swelling.

Over the past two decades of development, 19 different batches (i.e., heats) of 14YWT have been produced, and significant batch-to-batch variation has been noted between each heat as a function of varying extrusion ratios, milling parameters, impurity contents, and consolidation temperatures. This prior mechanical testing is summarized in a report by Hoelzer [3], and the mechanical data are reproduced in Figure 1. Four of these specific heats of 14YWT show the improvements made over the past 20 years. One of the initial heats, CR2, was produced in 2002 and shows the lowest high-temperature strength. The SM10 heat, produced in 2007, represents the highest strength heat of 14YWT ever produced, but it concurrently had the lowest ductility of all the heats. The SM13 heat, produced in 2013, provides arguably the most balanced set of strength and ductility performance parameters compared with any of its competitors [4]. The final heat, 14YWT-NFA1, produced in 2013, is by far the most widely researched 14YWT heat because of its larger mass; it was produced for research (5 kg), providing a good balance of strength and ductility [5, 6]. This was a unique heat because it attempted to gas atomize yttrium directly into the precursor reactive powder rather than adding Y_2O_3 to the powder separately.

Over the course of this optimization, the proficiency of Oak Ridge National Laboratory (ORNL) in controlling impurity elements (i.e., carbon and nitrogen) has improved considerably (Figure 2). Although it is not possible to use conventional missing processes to completely mitigate impurity elements such as carbon from the milling media and nitrogen from the impure milling atmosphere,milling , the levels are routinely below 1,000 ppmw, which has been shown to significantly improve fracture toughness in some of the more recent 14YWT heats [4]. It is important to note that the NFA1 alloy was milled by an external vendor (Zoz GmbH) rather than ORNL, which resulted in lower nitrogen levels than expected for scalable ODS production [6].

Even with these improvements in ODS processing, campaign initiatives, including expensive irradiations, continue to rely on the NFA1 heat, which is now a decade old and no longer reflects the state of the art in modern nanostructured alloy production. Furthermore, because of its unique additions of yttrium in the gas atomized powder, it is still unclear whether significant bimodalities noted in grain size and precipitate sizes [7, 8] are caused by the intrinsic heterogeneity of ODS alloy production or specific heterogeneities in the precursor gas-atomized powder used to produce the NFA1 heat. Consequently, this work outlines an effort to produce a new large-batch 14YWT heat, aptly named 14YWT-NFA2, for campaign testing in FY24. This material will eventually be irradiated through an international collaboration with Japan in their JOYO reactor in the late 2020's.

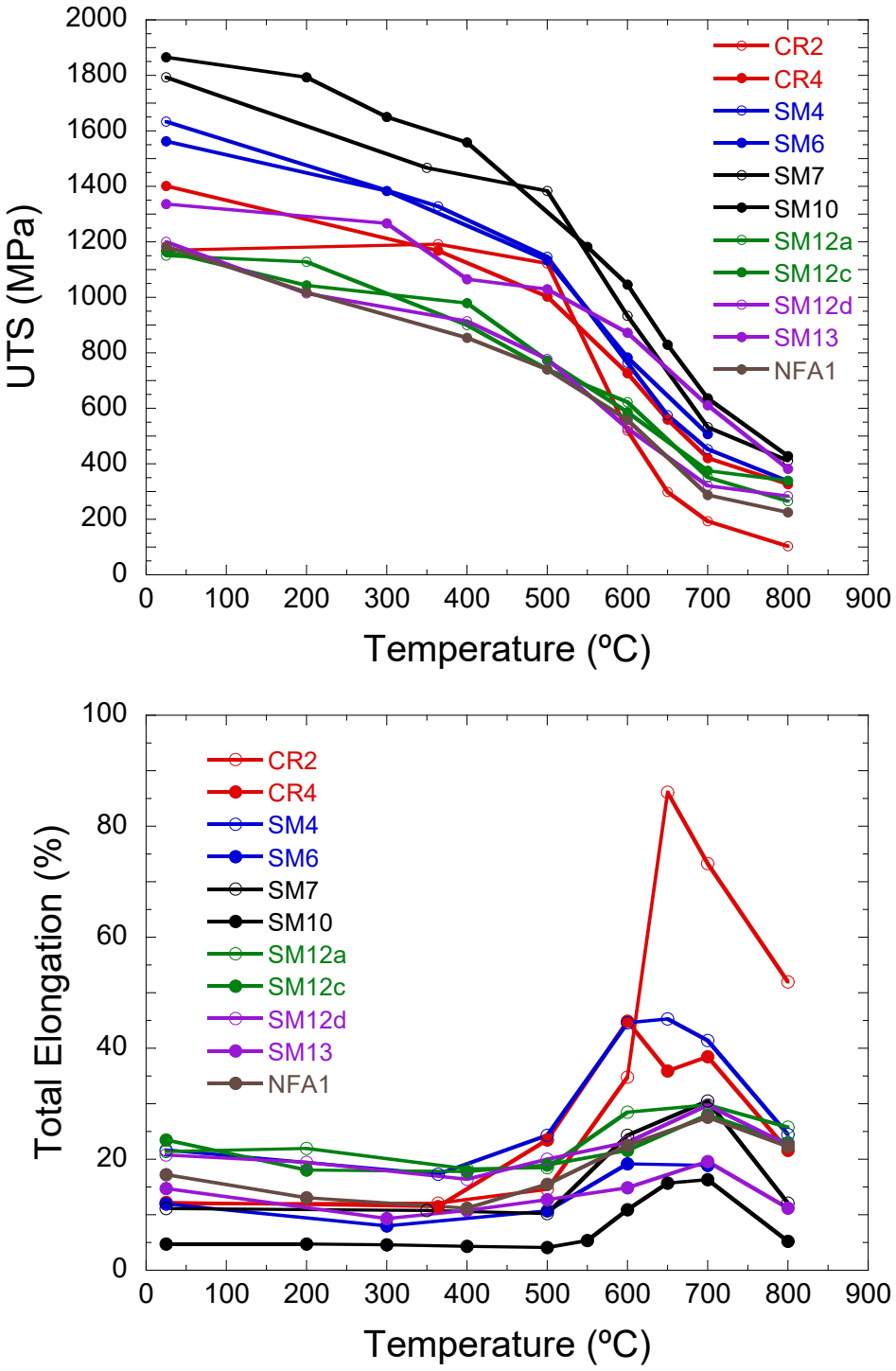

Figure 1. Comparison of ultimate tensile strength and total elongation from 25°C to 800°C for the 14YWT heats.

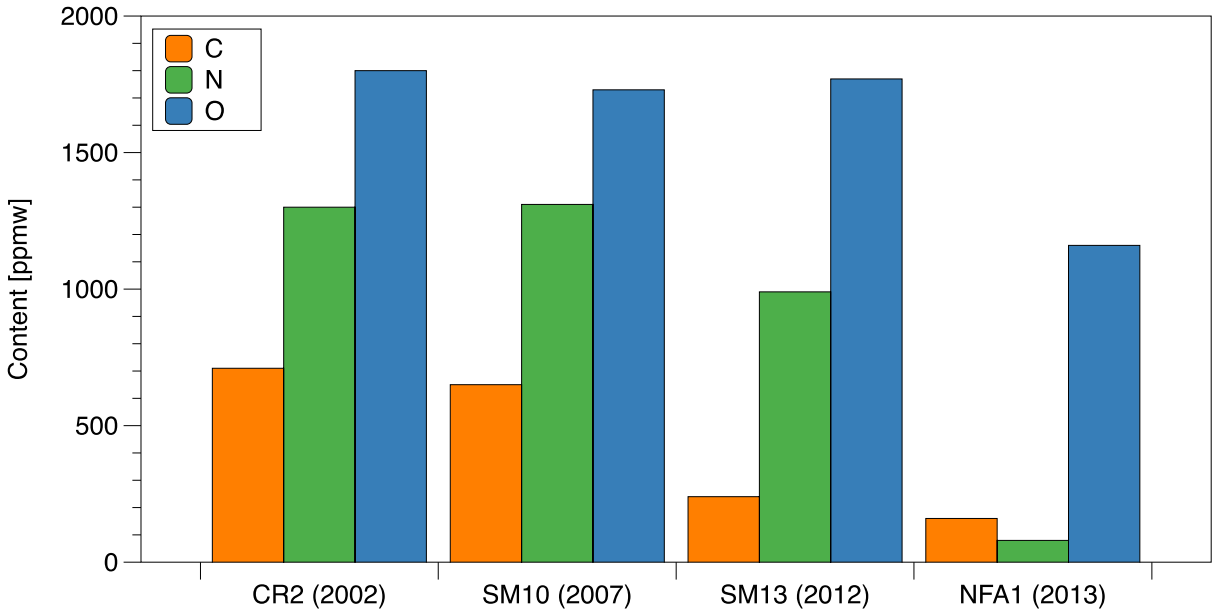

Figure 2. Impurity contents in select 14YWT heats. Label includes heat designation with the year of production in parentheses.

2. 14YWT Powder Production

During 14YWT production, different heats have been produced using powders provided by different vendors, including Special Metals (i.e., SM10 and SM13), Crucible Research (i.e., CR2), and ATI Powder Metals (i.e., NFA1). Unfortunately, these vendors are either no longer in business or unable to provide research quantities of powder. For example, during the COVID-19 pandemic, ATI Powder Metals closed their small-scale powder production plant and were no longer willing to provide research-scale quantities of powder to ORNL. For this campaign, precursor gas atomized 14YWT powder was procured from Powder Alloy Corporation based on the minimum and maximum allowable specifications listed in Table 1.

For this set of powder (lot # 26081001), carbon content was kept at 63 ppmw, nitrogen at 110 ppmw, and oxygen at 79 ppmw based on the material certification provided by the vendor. Methods used for elemental measurements ranged from inductively coupled plasma mass spectrometry (ICP-MS) or inductively coupled plasma optical emission spectroscopy (ICP-OES) for major element constituents, to either inert gas fusion (IGF) or combustion analysis for impurity element quantification. This low initial level of impurities is likely to result in better control in impurities during alloy production. In addition, silicon and aluminum (i.e., other reactive element oxide formers) were kept acceptably low at 210 ppmw and 150 ppmw to try and prevent additional grain boundary oxide formation, which has been shown to deteriorate fracture toughness in alloys such as MA957 [9]. The titanium content was at the lower end of acceptable limits, but this is not expected to significantly affect the precipitation of the complex yttrium-, titanium-, and oxygen-rich clusters throughout the alloy. A total of 100 kg is available for alloy production.

Table 1. 14YWT gas atomized powder specification

Element	Measured [wt%]	Min [wt%]	Max [wt%]	Method
Fe	bal	bal	bal	n/a
Cr	13.89	13.5	14.5	ICP-OES
W	2.97	2.8	3.2	ICP-OES
Ti	0.3	0.3	0.5	ICP-MS
Mn	0.074	0	0.075	ICP-MS
Al	0.024	0	0.025	ICP-MS
Si	0.021	0	0.025	ICP-MS
Ni	0.015	0	0.015	ICP-MS
N	0.011	0	0.02	IGF
P	0.008	0	0.015	ICP-MS
O	0.0079	0	0.05	IGF
C	0.0063	0	0.01	Combustion
S	0.004	0	0.015	Combustion

3. Mechanical Alloying

After the gas-atomized 14YWT powder was received at ORNL. Milling was performed using a Zoz Simoloyer model CM08 grinding unit equipped with a chamber capable of holding 1 kg batches of powder per run. A 10:1 ratio of mild steel milling media to mixed powder was used for all milling runs. The 14YWT powder mixture, comprising 997 g of gas atomized powder and 3 g of Y_2O_3 powder from Alfa Aesar (25–50 nm crystallite size), was loaded into the milling chamber with 10,000 g of milling media that had previously been used for 14YWT production to minimize carbon uptake from new milling media. The chamber was evacuated to 50–60 mTorr and backfilled to atmospheric pressure three times using ultra-high purity argon (Airgas PT# AR UHP300). The final backfill of argon was intentionally kept at an overpressure of 2 psig to help mitigate air ingress into the chamber.

After each milling run, which entailed 40 h of milling at rotational speeds ranging from 400 to 650 rpm at 8- and 4-minute increments, powder was extracted and placed in individual containers. During milling, the repeated fracture and cold welding of powder slowly mixes, fragments, and dissolves the Y_2O_3 into the matrix in a supersaturated solid solution, which enables the rapid nucleation of the complex yttrium-, titanium-, and oxygen-rich clusters during subsequent high-temperature consolidation. Thus, the morphology and size of the powders change during milling (Figure 3). The milled powder, which is flat and pancake-like in its morphology, is slightly broader in distribution than the initial spherical gas atomized powder, in which the initial average particle size 70 μm.

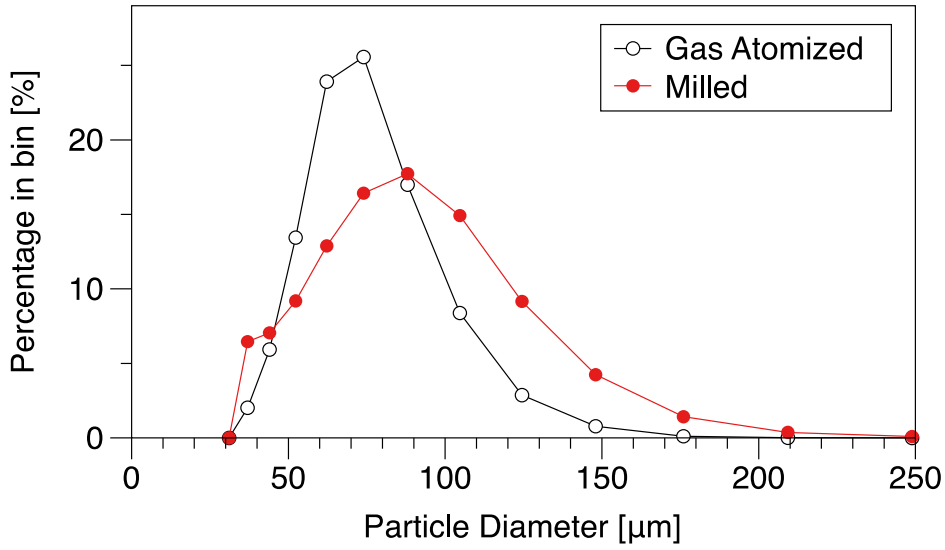

Figure 3. Characterization of representative particle size distributions before and after mechanical alloying.

4. Alloy Consolidation

As of this writing, 12 kg of milled 14YWT powder has been produced for eventual consolidation; 8 kg of this powder was packed extrusion cans having 4-inch outer diameters. The cans were degassed at 300°C for 24 h under high vacuum and were then subjected to high-temperature consolidation via extrusion after a two-step annealing procedure. The first stage of annealing, a 2 h anneal at 850°C, enabled the precipitation of a high density of NCs throughout the mechanically alloyed powder, whereas the second annealing step (and extrusion) at 1,000°C after 2 h provided alloys with optimized strength and ductility as a result of the additional energy for dislocation and grain boundary mobility during the high strain rate deformation and powder consolidation. Images of the four NFA-2 bars are shown in Figure 4. To expedite sample machining, the bars were sectioned near the middle of the material to avoid non-ODS mild steel can material near the nose and tail of each extruded bar. Future work will involve de-canning the material to preserve the pristine NFA for future rolling/annealing/machining operations.

Figure 4. Photo of four new 14YWT bars available for specimen machining.

5. Microstructural Characterization

Microstructural characterization of the new NFA-2 extruded heats included both larger length scale electron backscatter diffraction (EBSD) and lower length scale transmission electron microscopy (TEM). A TESCAN MIRA3 scanning electron microscope equipped with an Oxford Symmetry EBSD detector was used to perform EBSD; data were collected using an accelerating voltage of 20 kV and a step size of 50 nm. TEM data were collected using a JEOL JEM 2100F equipped with a 200 kV Schottky Field Emission Gun, and a Gatan Imaging Filter enabled energy-filtered transmission electron microscopy (EFTEM) capability.

Representative EBSD maps of each of the four extruded 14YWT NFA-2 bars are presented in Figure 5. Each set of images includes an inverse pole figure (IPF) map showing the preferred grain orientation perpendicular to the extrusion direction, with the extrusion direction oriented vertically in each image. A map of geometrically necessary dislocations (GNDs) calculated using the kernel average misorientation between neighboring voxels is included with the first IPF image. The GND density was calculated using the slip systems in the body-centered cubic lattice to accommodate changes in orientation within grains. Although statistically stored dislocations are not captured using this method, the maps show GND densities in the range of (3.6–4.8) × 10^{14} m^{-2}, which is within the regime expected for NFAs with dislocations pinned by nanoscale oxide features within the grains. Although the average grain sizes for the four 14YWT heats measured 3.0, 2.1, 3.9, and 4.9 μm for NFA-1, 2, 3, and 4, respectively, it the larger grain size is likely explained by the cleaner variation of these heats in comparison with those in the legacy material.

Nanometer scale analysis of the microstructure confirms both the high dislocation density and the high number density of NCs strengthening the material. TEM bright field (BF) micrographs showing the microstructure of 14YWT-NFA2 (third extruded heat) are shown in Figure 6. At low magnifications (Fig. 1a), contrast from long-range strains caused by dislocations in the matrix are visible. Large second-phase particles were not observed in the matrix or on grain boundaries during the inspection of the thin lamella specimen. Even at high magnifications (Figure 6b), no contrasts from second-phase particles were detected in the BF micrograph. Additional TEM analysis will be conducted on thin lamella specimens prepared from the other extruded heats to verify the BF characterization of the microstructure.

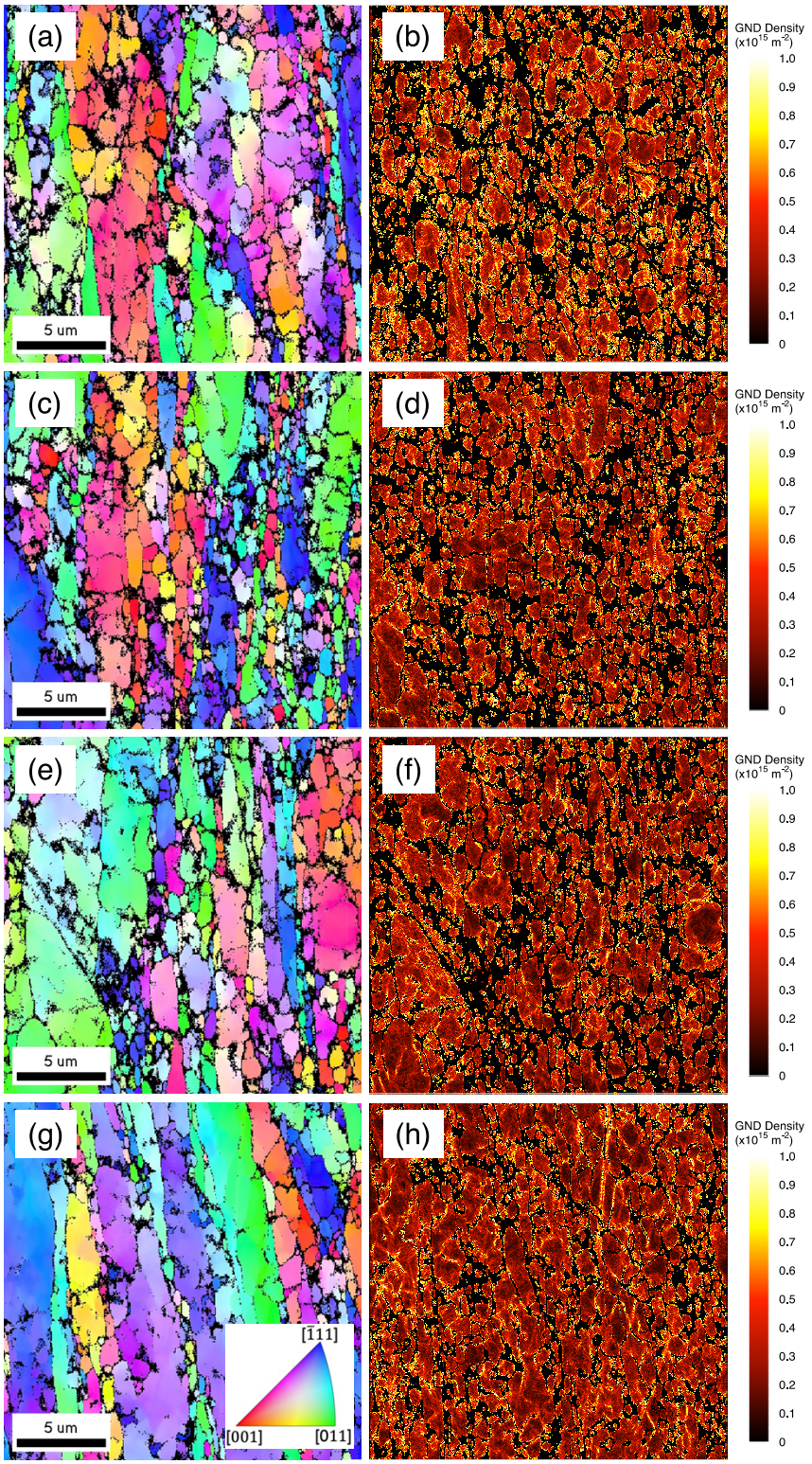

Figure 5. EBSD inverse pole figure (left) and GND density (right) maps for extruded heats NFA2-1 (a, b), NFA2-2 (c, d), NFA2-3 (e, f) and NFA2-4 (g, h).

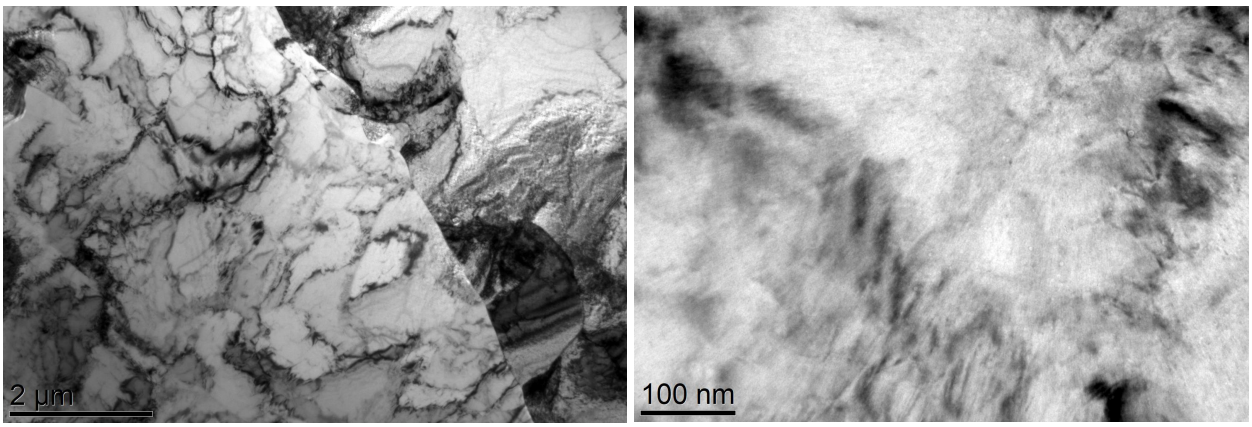

(a) (b)

Figure 6. TEM Bright Field micrographs showing the microstructure of 14YWT-NFA2 at (a) low magnification and (b) high magnification.

Results from past studies on characterization of the nano-size Ti-Y-oxygen-enriched NCs in 14YWT show that EFTEM jump-ratio maps of the inner-shell ionizations of elements are the most reliable imaging method [10]. The results of EFTEM jump-ratio maps obtained from the thin lamella specimen of 14YWT are presented in Figure 7a (Fe-M jump-ratio map) and Figure 7b,(Ti-M jump-ratio map), respectively. The Fe-M jump-ratio map shows a high concentration of particles with dark contrast; these particles correspond to those showing bright contrast in the Ti-M jump-ratio map. The presence of Ti in the same location as the particles with dark contrast is consistent with Y-Ti-O NCs. The dark contrast indicates that Fe atoms are displaced locally from the NCs. Typically, the Fe-M jump-ratio map shows better spatial resolution than the Ti-M jump-ratio map. Figure 7c shows the t/λ thickness map obtained at the same magnification and region of the microstructure as the Fe-M and Ti-M jump-ratio maps. The specimen thickness, *t*, is determined from the t/λ map, which was obtained as follows:

$$t/\lambda = \ln(\text{unfiltered image}/\text{zero loss image}),$$

where λ is the inelastic scattering mean free path, which for Fe was determined to be ~105 nm based on the collection angle β = 10 mRad. The average thickness of the analyzed region in the t/λ map was ~18 nm. The resolution achievable in the jump-ratio maps depends on the specimen thickness. Figure 7d illustrates this with the line intensity profile across the NC (blue line inset in the Fe-M jump-ratio map of Figure 7a), which shows that the size of this NC is 1.85 nm diameter at full-width, half-maximum (FWHM).

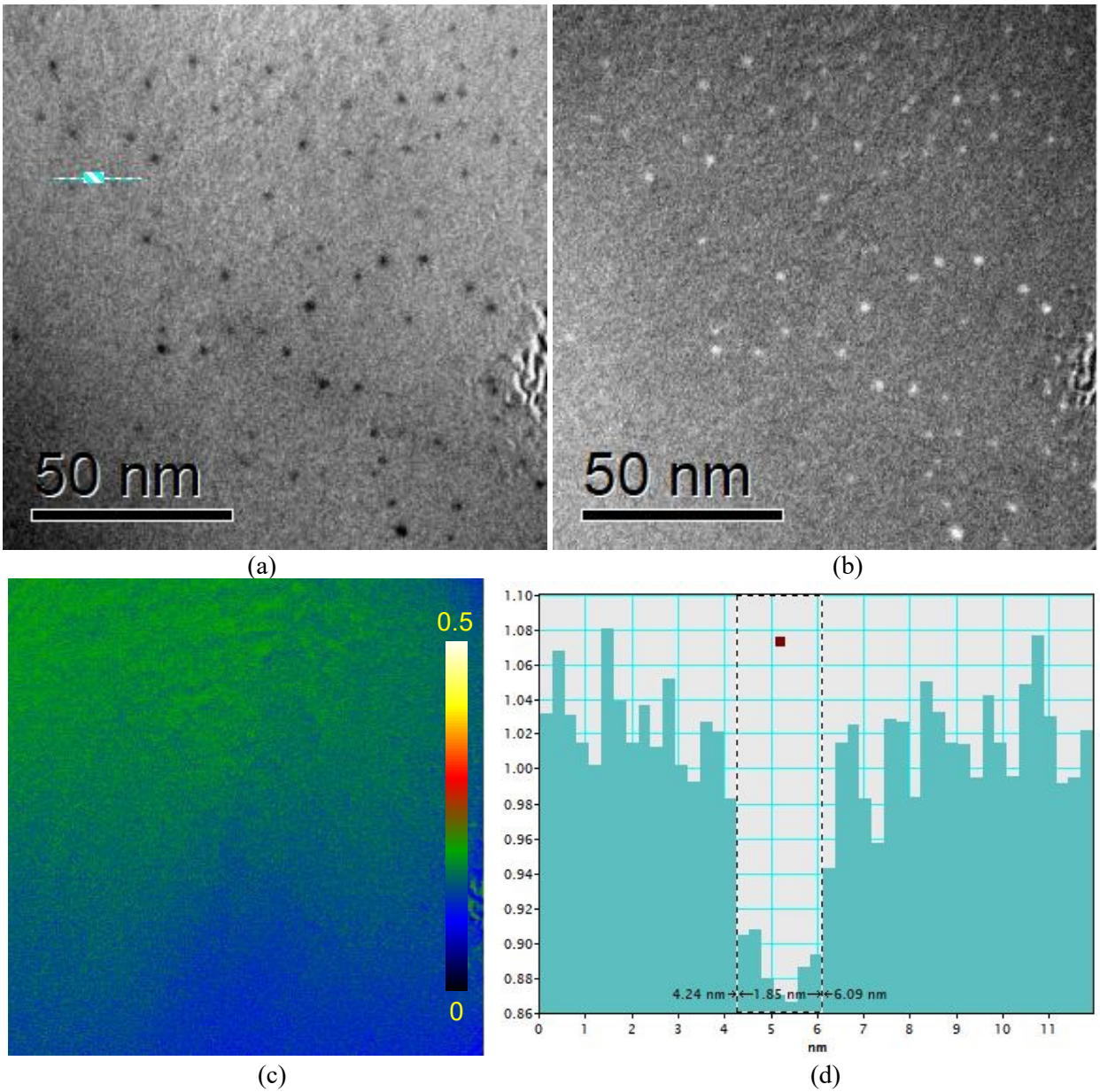

Figure 7. Results of the EFTEM analysis of 14YWT-NFA2 region 1. (a) Fe-M jump-ratio map, (b) Ti-M jump-ratio map, (c) t/λ thickness map, and (d) line intensity profile of the NC observed in Fig. 7a with the blue line inset.

Figure 8 shows the results of the EFTEM analysis in the thin lamella specimen from a different region than the one shown in Figure 7. The Fe-M and Ti-M jump-ratio maps of the second region, shown in Figure 8a and Figure 8b, respectively, have a higher number of NCs. As previously explained in this section, particles show dark contrast in the Fe-M jump-ratio map and bright contrast in the Ti-M jump-ratio map. The larger coverage of red in the t/λ thickness map in Figure 8c indicates that this region is thicker than the one shown in Figure 7. The average thickness of the t/λ map in this region was ~24 nm. Figure 8d shows the line intensity profile across the NC (blue line inset in the Fe-M jump-ratio map of Figure 8a) indicating a size of 1.88 nm diameter at FWHM.

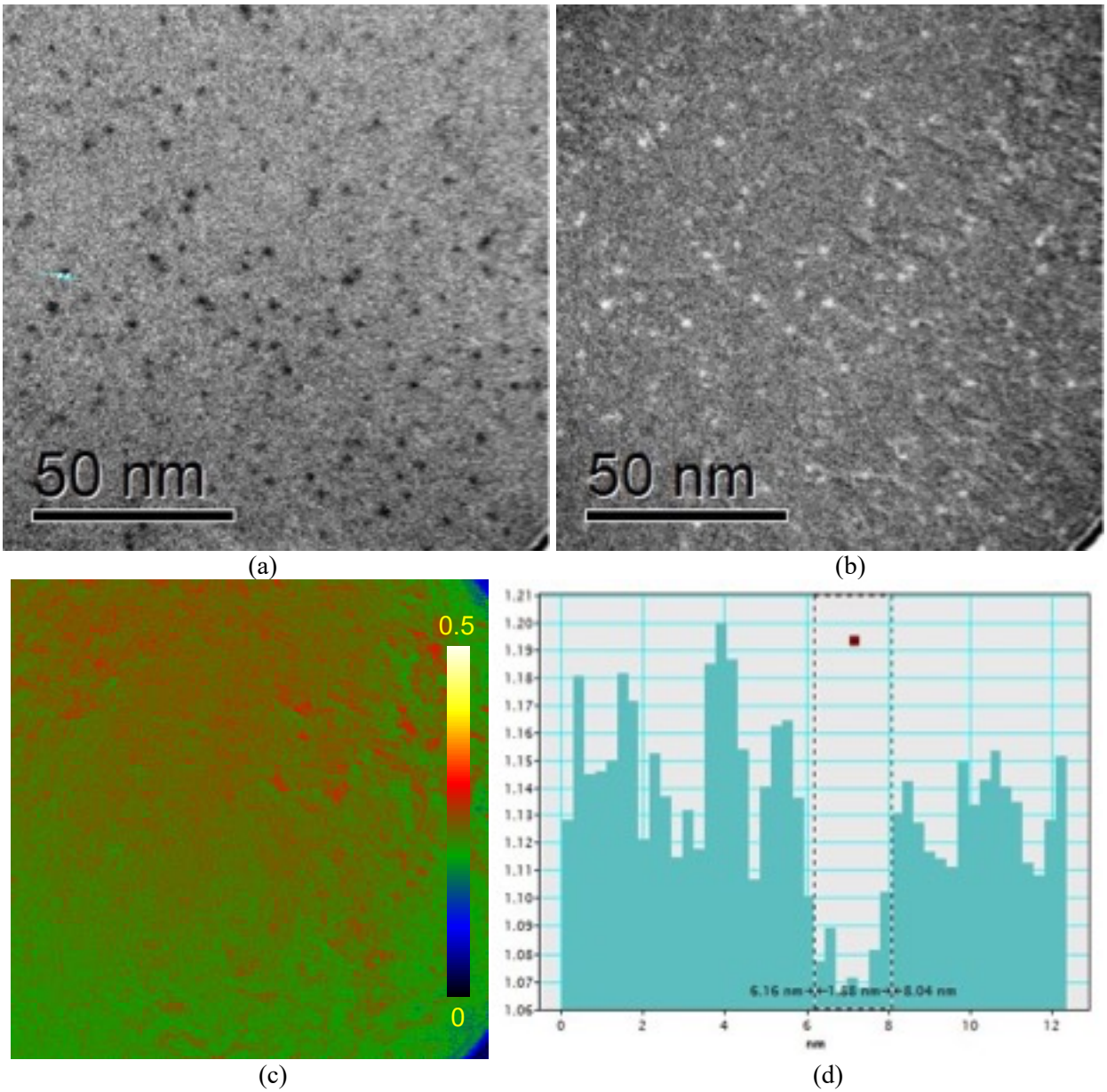

Figure 8. Results of the EFTEM analysis of 14YWT-NFA2 region 2. (a) Fe-M jump-ratio map, (b) Ti-M jump-ratio map, (c) t/λ thickness map, and (d) line intensity profile of the NCs observed in Fig. 8a with the blue line inset.

The size analysis of the NCs observed in the Fe-M jump-ratio maps in the previous figures was conducted using Image J software (version 1.4.3.67). Figure 9 illustrates the procedure of the Image J analysis. The Fe-M jump-ratio map is opened in Image J, the scale obtained from the map is set, and a region of interest (ROI) is selected from the Fe-M jump-ratio map and a duplicate map is generated (Figure 9a). A fast Fourier transform (FFT) bandpass filter with a range of 20% to 40% is applied to the ROI map. Then the threshold setting is applied to the ROI map to obtain the black contrast for the NCs on a white background as shown in the matrix (Figure 9b). The NCs are then analyzed using the particle analysis tool in Image J, which calculates the area of each NC and creates an outline of the area for each NC that is compiled in an Excel spreadsheet. The diameter is calculated from the area of the NC assuming a spherical morphology. The average diameter and standard deviation of the NCs are obtained. The NCs <1 nm in diameter identified by Image J were not included in the calculation of the average size and standard

deviation. The procedure using Image J to assess the average size of the NCs was performed on the two Fe-M jump-ratio maps shown in Figure 7a and Figure 8a, which will be referred to as ROIs #1 and #2, respectively, in the following results.

The average size and the number of NCs present in ROIs #1 and #2 were obtained in the Image J analysis. The number density of NCs was obtained by multiplying the average thickness of ROIs #1 and #2 as determined from the t/λ thickness maps shown in Figure 7c and Figure 8c, with the area calculated for ROIs #1 and #2 of the Fe-M jump-ratio maps. Table 2 shows the number of NCs counted, the average thickness, average size, and the number density determined from the EFTEM results and the Image J analysis of ROIs #1 and #2. The results showing that a higher number of NCs were present in ROI #2 compared to ROI #1 is caused by the greater thickness of ROI #2. The results showed very good agreement between the average size of NCs in ROIs #1 and #2. However, the number of NCs calculated for ROI #2 was slightly more than 2× that of ROI #1. The reason for this is not clear, but it may be influenced by errors estimated for the average thickness of ROIs #1 and ROI #2 caused by variations in thickness gradients, as well as by sampling errors because the ROIs analyzed here were small. Size distribution histograms of the NCs were obtained from the Image J analysis of ROIs #1 and #2 and are shown in Figure 10. Both histograms show a small range of peak diameters in NC size frequency, between ~1.5 and 3.0 nm, which is considered a very good result that confirms the mechanical alloying processing conditions used for producing the new 14YWT-NFA2 heats.

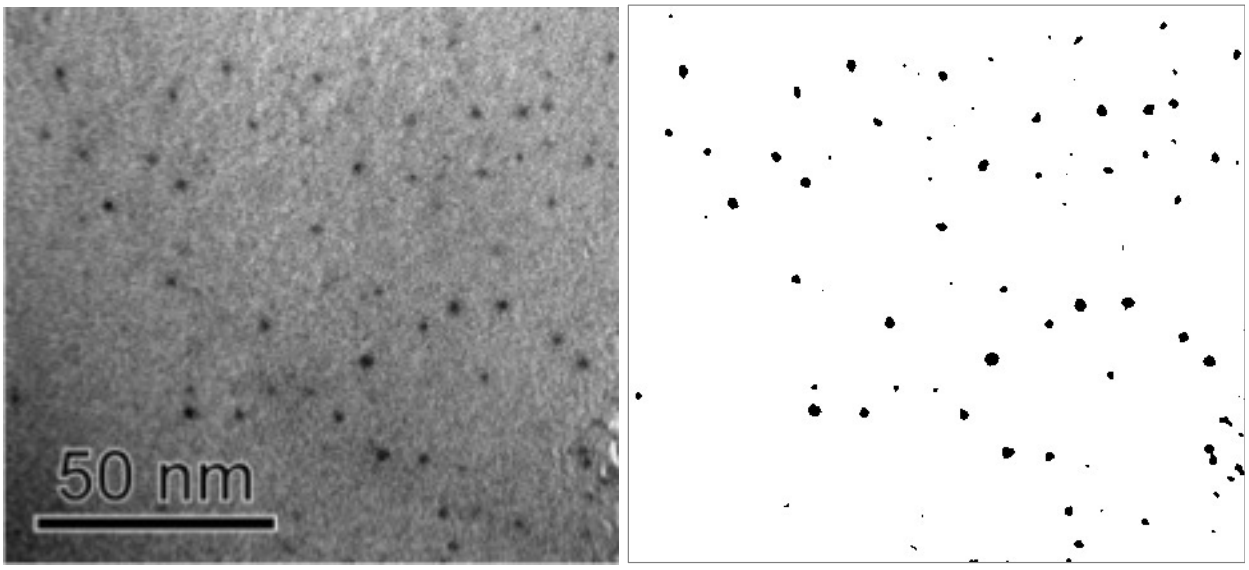

(a) (b)

Figure 9. Results from procedure used in the Image J analysis of NCs observed in the Fe-M jump-ratio map of 14YWT presented in Figure 2a. (a) Duplicate image of the ROI containing the NCs, and (b) threshold image of the NCs showing black contrast on a white background.

Table 2. Summary of nanoclusters identified in ROIs #1 and #2 with average thickness, average size, and number density of NCs determined from the EFTEM results and Image J analysis

ROI	Number Counted	Average Thickness	Average Size	Number Density
#1	51	18.3 nm	1.880 +/- 0.433 nm	$1.86 \times 10^{23}/m^3$
#2	148	24.2 nm	1.868 +/- 0.593 nm	$3.86 \times 10^{23}/m^3$

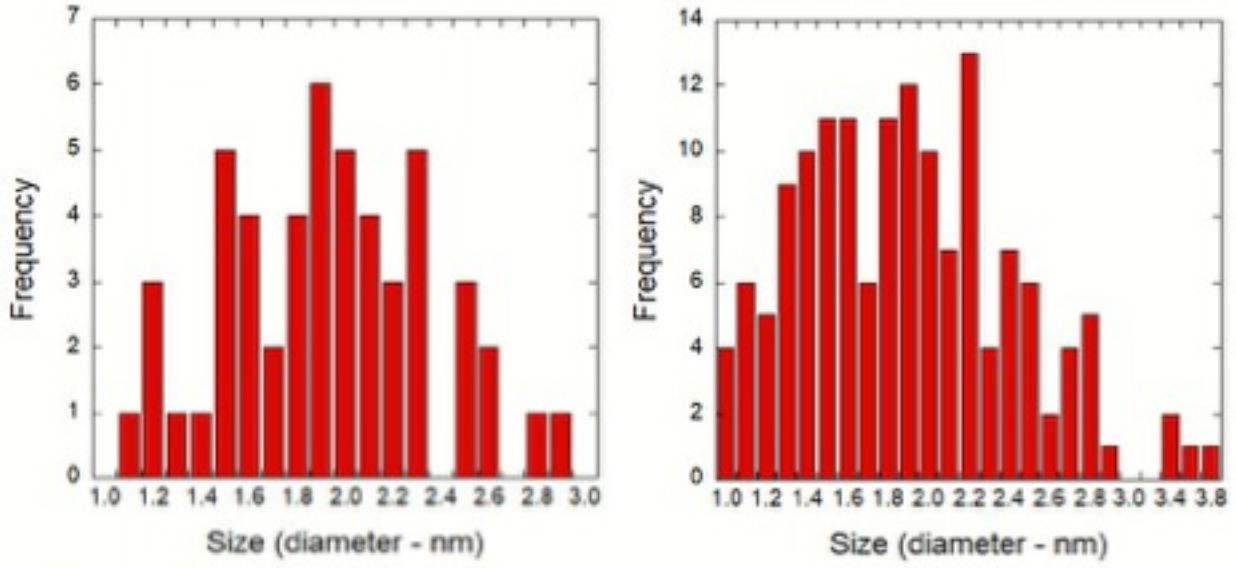

(a) (b)

Figure 10. Size distribution histograms of NCs observed in the Fe-M jump-ratio maps shown in (a) Figure 2a and (b) Figure 3a.

6. High-Temperature Mechanical Properties

High-temperature mechanical properties were generated for each of the four 14YWT NFA-2 bars using subsized SS-J2 tensile specimens. These specimens have a gauge length of 5 mm, a width of 1.2 mm, and a thickness of 0.5 mm. Although subsized specimens are not ideal for establishing properties such as total elongation in comparison with standard-sized specimens consistent with ASTM standards, they are a useful screening tool for establishing properties such as yield strength, ultimate tensile strength, and uniform elongation. Mechanical testing was performed in air at temperatures of 23, 200, 400, 600, and 800°C using a strain rate of 10^{-3} s^{-1}. An Instron mechanical test frame with a 5 kN load cell and a custom induction-heating setup was used to control sample temperature, and each sample was held for 10 minutes at the test temperature to ensure uniform temperature prior to beginning the tensile test. After sample fracture, the engineering stress/strain curves were adjusted to subtract the elastic deformation of the sample, as well as the machine and fixture compliance, leaving only the sample stress and plastic strain. This approach established accurate strength and ductility properties.

A summary of the individual compliance-corrected tensile tests is presented in Figure 11, with temperatures ranging from room temperature up to 800°C. Generally, all four extruded bars exhibited high room temperature ultimate tensile strength (~1,200 MPa) without sacrificing ductility (uniform elongation ~7%). As the temperature increased marginally to 200°C, all four bars retained their consistent performance. Unfortunately, as temperature increased, the uniform elongation steadily decreased for the nanostructured 14YWT alloy. At 600°C, the alloy had approximately 1% strain hardening capacity prior to the onset of necking and localized plastic deformation.

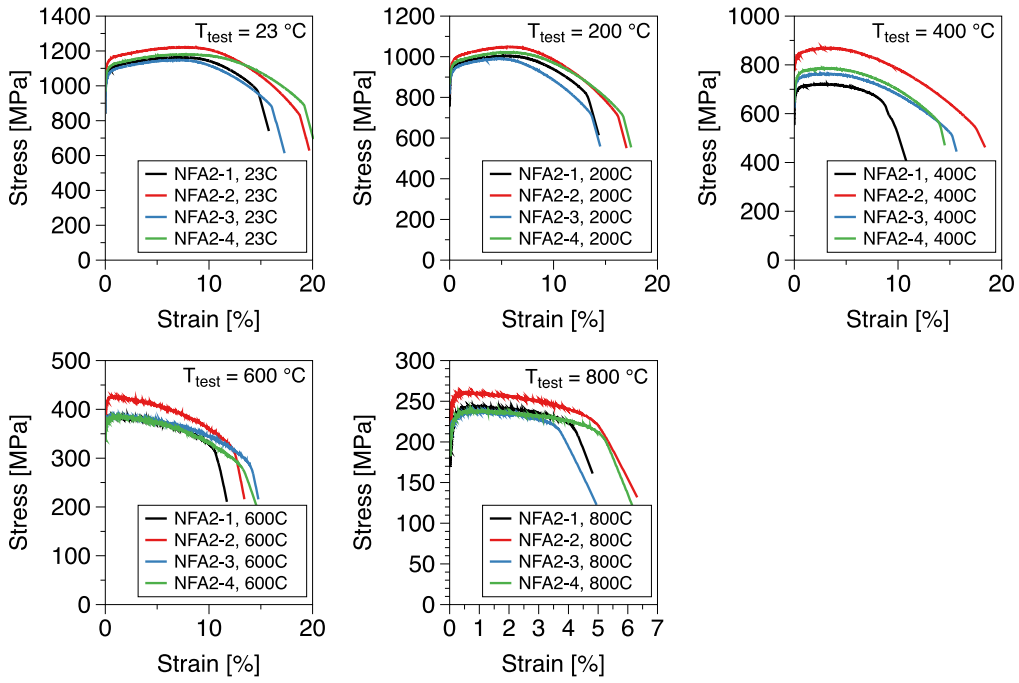

Figure 11. Compliance-corrected engineering stress vs. plastic strain curves for specimens extracted from four rectangular bars from the new 14YWT NFA-2 heat, tested from 23–800°C.

Although the ductility decreased for these alloys as a function of the increasing test temperature, a metadata analysis of the mechanical properties confirmed that these alloys perform in a superior manner in comparison to prior legacy heats of 14YWT. For example, the impurity level of the high-strength SM10 heat was quite high, especially in carbon and nitrogen. The current cleaner NFA-2 heats have much fewer impurities which can be seen in Figure 12 by comparing the measured C, N, and O levels in the NFA-2 heats with those legacy heats.

This decrease in impurity content, coupled with optimized annealing and extrusion conditions, has a drastic effect on strength and ductility, as summarized in the comparative analysis of tensile data in Figure 13. At temperatures below 600°C, the NFA-2 alloys have higher uniform elongation than the previous SM10 heat, whereas total elongation is comparable, even at these elevated temperatures. In addition, although the strength values are lower than those of SM10, these new, cleaner NFA-2 heats still have yield and ultimate tensile strengths above 1 GPa at room temperature, and they retain yield strength and ultimate tensile strength values in the 200–250 MPa range at temperatures up to 800°C.

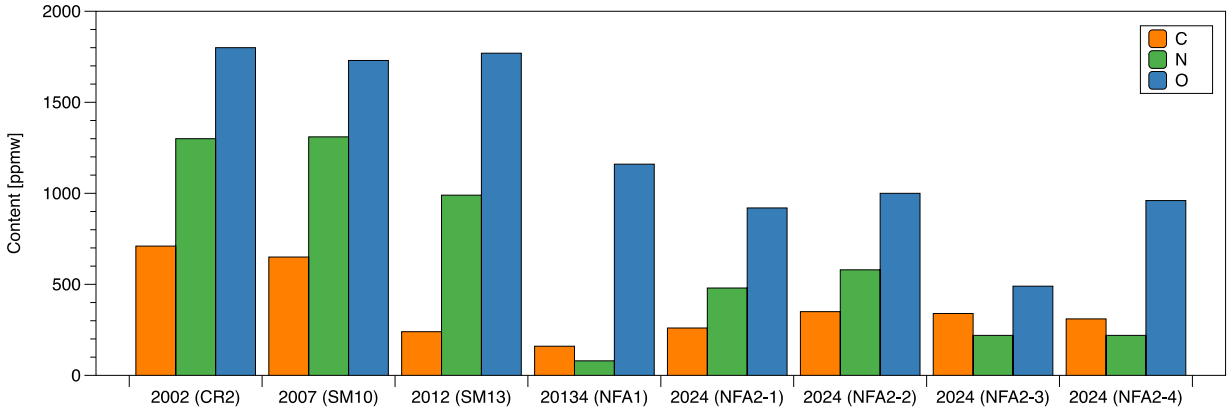

Figure 12. Measured impurity levels in new 14YWT NFA-2 heats vs. previous heats from Figure 2.

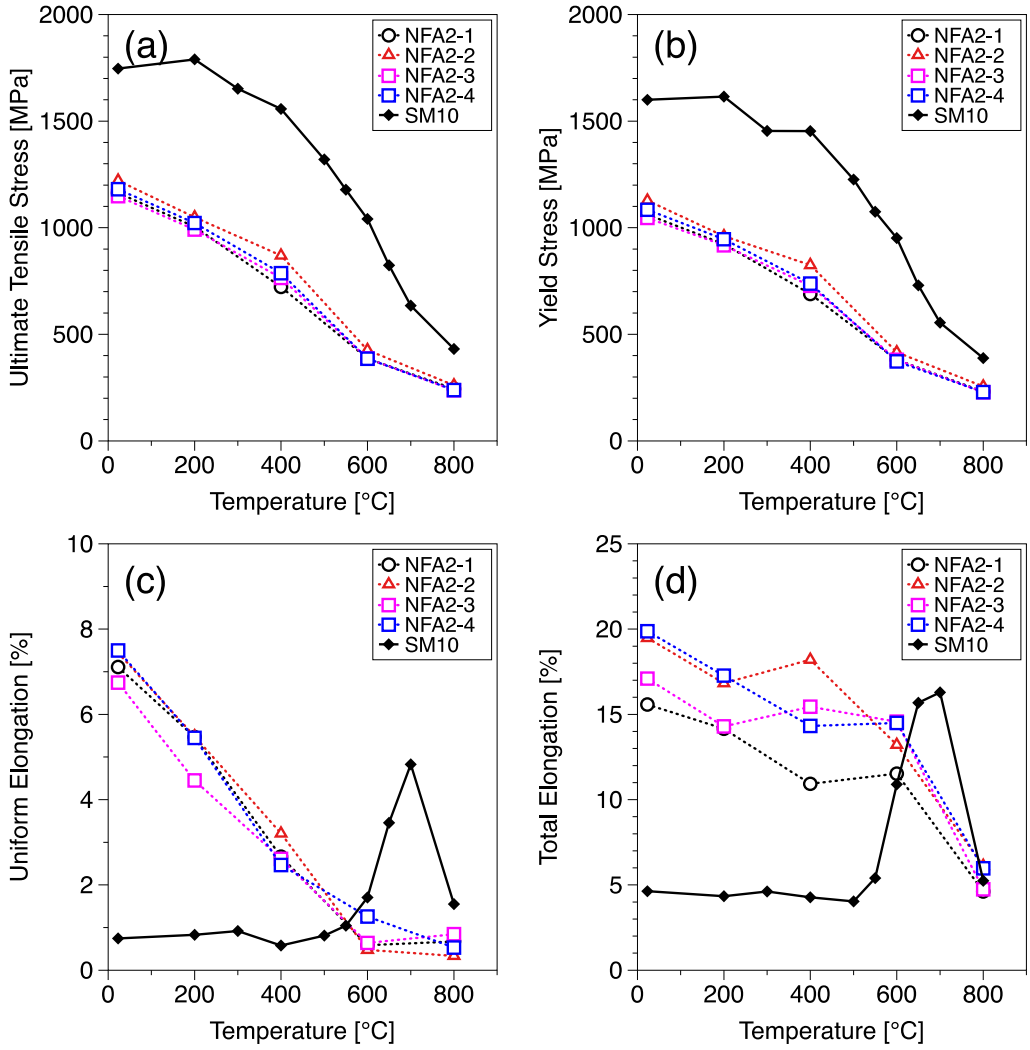

Figure 13. Summary of high-temperature properties for 14YWT NFA-2 bars, including (a) ultimate tensile strength, (b) yield strength, (c) uniform elongation, and (d) total elongation.

7. Conclusion

Based on the literature about previous 14YWT heats, it is clear that significant variability exists in the performance metrics of this nanostructured ferritic alloy, depending on impurity control and prior processing history. Therefore, with the noted improvements in process control and thermomechanical processing conditions, having a new best-practice heat of 14YWT for campaign testing is required to ensure that data resulting from irradiations are representative of the state of the art for this class of alloys. Four new rectangular bars have been fabricated with lower impurity contents for Advanced Fuels Campaign irradiation testing, each having a combination of simultaneously high tensile strength and ductility. Although the reduced impurity content and higher extrusion temperature resulted in larger grain sizes, the fine distribution of (Y,Ti,O)-rich nanoprecipitates was preserved, which succeeded in pinning dislocations and increasing the effective dislocation density. Rectangular plates will be used for future rolling, annealing, and weld studies. In addition, plans are still in place to extrude at least five circular rods with nominal dimensions of 1.25 in. outer diameter and lengths ranging from 12 to 24 in. length. When previous bar stock of this length is reduced down using pilgering to fast reactor cladding dimensions, the result was a tube lengths approaching or exceeding 2 m.

8. References

[1] J.H. Kim, T.S. Byun, D.T. Hoelzer, S.-W. Kim, B.H. Lee, Temperature Dependence of Strengthening Mechanisms in the Nanostructured Ferritic Alloy 14YWT: Part I—Mechanical and Microstructural Observations, Materials Science and Engineering: A 559 (2013) 101–110.

[2] D.A. McClintock, D.T. Hoelzer, M.A. Sokolov, R.K. Nanstad, Mechanical Properties of Neutron Irradiated Nanostructured Ferritic Alloy 14YWT, Journal of Nuclear Materials 386–388 (2009) 307–311.

[3] D.T. Hoelzer, Summary of Previous Mechanical Test Data on ODS Alloys 14YWT and OFRAC up to 1000ºC, Oak Ridge National Lab.(ORNL), Oak Ridge, TN (United States); USDOE …, 2021.

[4] D.T. Hoelzer, K.A. Unocic, M.A. Sokolov, T.S. Byun, Influence of Processing on the Microstructure and Mechanical Properties of 14YWT, Journal of Nuclear Materials 471 (2016) 251–265.

[5] M.E. Alam, S. Pal, K. Fields, S.A. Maloy, D.T. Hoelzer, G.R. Odette, Tensile Deformation and fracture Properties of a 14YWT Nanostructured Ferritic Alloy, Materials Science and Engineering: A 675 (2016) 437–448.

[6] N. Cunningham, Y. Wu, G. Odette, D. Hoelzer, S. Maloy, Characterization of a Larger Best Practice Heat of 14YWT in Annealed Powder, HIP Consolidated and Extruded Forms, Fusion Materials Semiannual Progress Report for Period Ending June 30 (2013) 15–26.

[7] E. Aydogan, E. Martinez, K. March, O. El-Atwani, D.L. Krumwiede, P. Hosemann, T. Saleh, S.A. Maloy, Alpha' Formation Kinetics and radiation Induced Segregation in Neutron Irradiated 14YWT Nanostructured Ferritic Alloys, Sci Rep 9(1) (2019) 8345.

[8] E. Aydogan, J.S. Weaver, U. Carvajal-Nunez, M.M. Schneider, J.G. Gigax, D.L. Krumwiede, P. Hosemann, T.A. Saleh, N.A. Mara, D.T. Hoelzer, B. Hilton, S.A. Maloy, Response of 14YWT Alloys under Neutron Irradiation: A Complementary Study on Microstructure and Mechanical Properties, Acta Materialia 167 (2019) 181–196.

[9] M.J. Alinger, G.R. Odette, G.E. Lucas, Tensile and Fracture Toughness Properties of MA957: Implications to the Development of Nanocomposited Ferritic Alloys, Journal of Nuclear Materials 307–311 (2002) 484–489.

[10] J. Bentley, D. Hoelzer, D. Coffey, K. Yarborough, EFTEM and Spectrum Imaging of Mechanically Alloyed Oxide-Dispersion-Strengthened 12YWT and 14YWT Ferritic Steels, Microscopy and Microanalysis 10(S02) (2004) 662–663.